Lithium- and Magnesium-Storage Mechanisms of Novel Hexagonal NbSe₂

Chen Peng, Haoying Lyu, Lu Wu, Tengfei Xiong, Fangyu Xiong, Ziang Liu, Qinyou An,* and Liqiang Mai*

State Key Laboratory of Advanced Technology for Materials Synthesis and Processing, International School of Materials Science and Engineering, Wuhan University of Technology, Luoshi Road 122, Wuhan, 430070 Hubei, China

S *Supporting Information*

ABSTRACT: As a novel and potential transition metal dichalcogenide (TMDC), NbSe₂ has low ion diffusion barrier when applied in energy-storage systems, such as traditional lithium-ion batteries and novel magnesium-ion batteries (MIBs). In this work, we have developed a novel hexagonal NbSe₂ material with a nanosized surface via a facile microwave−hydrothermal method. The Li⁺-storage mechanism of NbSe₂ with surface conversion and internal intercalation is thoroughly revealed by in situ X-ray diffraction (XRD), ex situ high-resolution transmission electron microscopy, and ex situ scanning electron microscopy. Besides, Mg²⁺ intercalation mechanism is confirmed via ex situ XRD and ex situ X-ray photoelectron spectroscopy for the first time. In addition, as the cathode for MIBs, NbSe₂ with a nanosized surface exhibits a high rate capacity of 101 mA h g⁻¹ at 200 mA g⁻¹ with a high discharge plateau at 1.30 V. Our work builds a deep understanding of ion-storage mechanisms in TMDCs and provides guidance for designing new electrode materials with high electrochemical performances.

KEYWORDS: NbSe₂, transition metal dichalcogenides, lithium and magnesium storage mechanisms, magnesium ion batteries, microwave-assisted synthesis
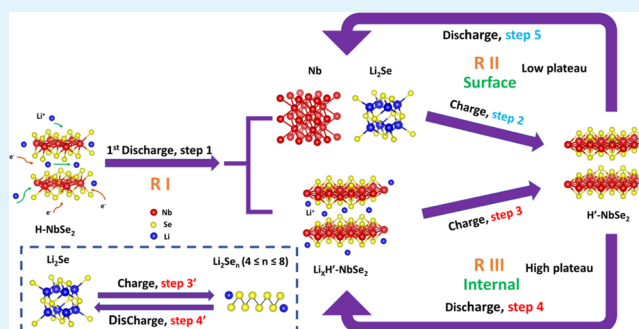
■ INTRODUCTION

Electrochemical energy storage (EES) becomes increasingly important because of the rapid consumption of fossil fuels and the large-scale development of low-cost, clean, and stable electric energy.[1−5] As a typical EES device, lithium-ion batteries (LIBs) have been powering most of the portable electronic devices for several decades owing to their high energy density and long cycle life.[6,7] Magnesium-ion batteries (MIBs), as another battery prototype, also attracted great attention recently because of their high volumetric energy density, high safety, and low cost.[8−11] Transition metal dichalcogenides (TMDCs) used as the electrode material have been explored for many years because of their two-dimensional layered structure and weak interlayer van der Waals forces, which are propitious to lithium and magnesium storage.[12−17] To further develop kind of materials, deep investigations about the ion-storage mechanisms in these materials are necessary.

NbSe₂, as one of the attractive TMDCs, has received wide attention in research because of its superconductivity and charge density wave transition at low temperatures,[18−21] but little exploration has been done in LIBs and MIBs. In fact, the great application potential of this material for Li storage because of its low diffusion barrier has been predicted by Lv et al.[22] based on the first-principles calculation. As far as we

know, NbSe₂ was recently applied in LIBs only by Hitz et al. but without any investigation of the ion-storage mechanism.[23] To further promote the development of NbSe₂ electrode material in EES and provide guidance for designing new electrode systems for high-performance LIBs and MIBs, the Li⁺- and Mg²⁺-storage mechanisms in NbSe₂ should be thoroughly investigated.

Herein, a novel hexagonal NbSe₂ is facilely synthesized via microwave−hydrothermal method for the first time. Li⁺-storage mechanism of NbSe₂ with surface conversion and internal intercalation is first thoroughly proved by in situ X-ray diffraction (XRD), ex situ high-resolution transmission electron microscopy (HRTEM), and ex situ scanning electron microscopy (SEM). Besides, the Mg²⁺ intercalation mechanism is also confirmed via ex situ XRD and ex situ X-ray photoelectron spectroscopy (XPS). Meanwhile, after microwave treatment, NbSe₂ exhibits a superior high rate capacity of 101 mA h g⁻¹ at 200 mA g⁻¹ with a high discharge plateau around 1.30 V in coin-type MIBs with all phenyl complex (APC) as the electrolyte and Mg metal as the anode.
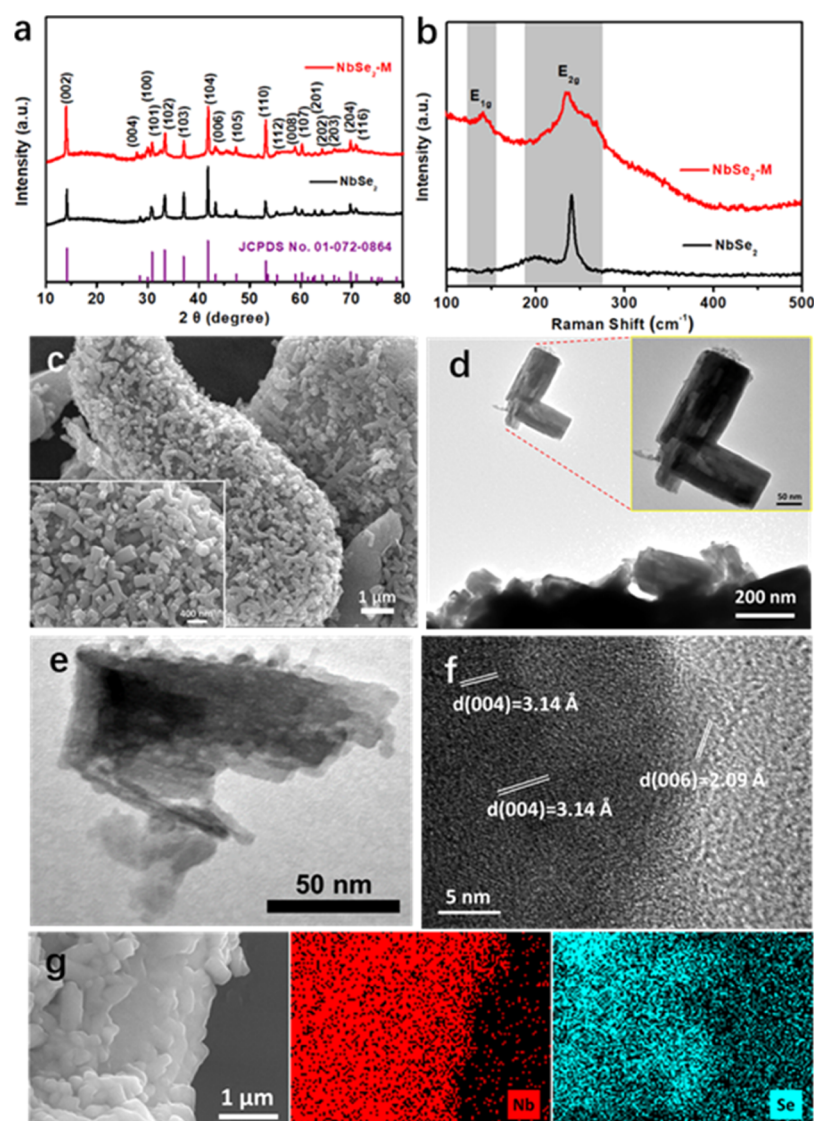
Figure 1. Structural and morphological characterizations of NbSe$_2$ and NbSe$_2$-M. XRD patterns (a) and Raman spectra (b) of NbSe$_2$ and NbSe$_2$-M. SEM (c), TEM (d,e), and HRTEM (f) images of NbSe$_2$-M. (g) SEM image and its corresponding EDS elemental maps of NbSe$_2$-M.

■ EXPERIMENTAL SECTION

Synthesis of NbSe$_2$ with a Nanosized Surface. Typically, 0.1 g of dark gray NbSe$_2$ bulk (Nanjing MKNANO Tech. Co., Ltd., 99.95%) was added to 30 mL of deionized water followed by ultrasonic treatment and fiercely stirring to be fully dispersed and dissolved. Then, the acquired suspension was transferred into a special Teflon-lined autoclave and subjected to microwave hydrothermal treatment in a XH-300UL+ ultrasonic ultraviolet light synthesis detector with a two-step process of being kept at 100 °C for 5 min, followed by being maintained at 180 °C for 12 h (heating rate: 10 °C min^{-1}) along with stirring in the whole process. The pressure and power were required to be lower than 4 MPa and 600 W, respectively. After natural cooling to room temperature and washing with deionized water and alcohol several times, the collected precipitation was dried at 80 °C in vacuum to obtain the final black product (noted as NbSe$_2$-M).

Material Characterization. XRD patterns of the products were recorded on a Bruker D8 ADVANCE X-ray diffractometer with a non-monochromatic Cu Kα X-ray source to characterize the crystallographic information. Raman spectra were employed for internal chemical bond information using a Horiba Scientific LabRAM HR Evolution Raman microscope. SEM images and energy-dispersive spectroscopy (EDS) elemental maps were obtained using a JEOL-7100F SEM/EDS microscope. TEM and HRTEM images were recorded by JEM-1400 and JEM-2100F electron microscopes, respectively. XPS measurement was employed with a VG Multi Lab 2000 instrument.

Electrochemical Measurements. The electrochemical performance was tested at room temperature (25 °C) by assembling CR2016-type coin cells in a glovebox filled with pure argon gas (O$_2$ ≤ 1 ppm and H$_2$O ≤ 1 ppm). For LIBs, NbSe$_2$-M was used as the cathode, lithium foil as the anode, and 1 M LiPF$_6$ in ethylene carbonate/dimethyl carbonate/ethyl methyl carbonate = 1:1:1 (vol %) as the electrolyte. For MIBs and magnesium–lithium hybrid batteries (MLHBs), NbSe$_2$-M was used as the cathode, Mg foil as the anode, 0.25 M APC and 1 M LiCl in 0.25 M APC as electrolyte. A Whatman glass fiber (GF/D) was used as the separator. The electrodes were fabricated to form a circular film with 60 wt % sample as the active material, 30 wt % acetylene black, and 10 wt % poly tetra fluoroethylene (PTFE) using a roller mill and then dried in an oven for over 12 h at 70 °C. The mass loading was about 5−7 mg cm^{-2}. Galvanostatic charge−discharge (GCD) profiles were measured through a multichannel battery testing system (LAND CT2001A). Cyclic voltammetry (CV) measurements were carried out at an electrochemical workstation (Autolab PGSTAT 302).
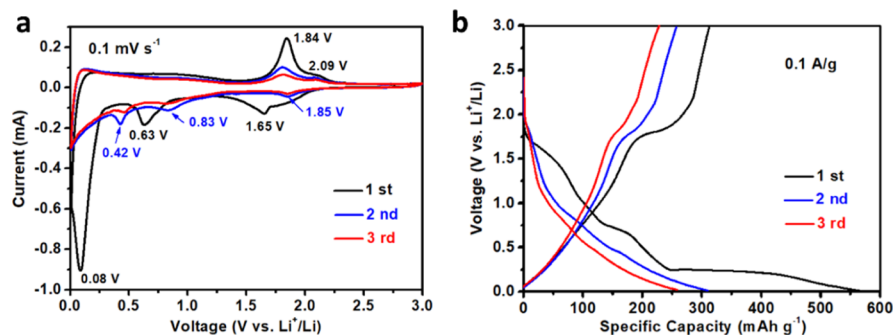
Figure 2. CV curves of the initial three cycles under the scan rate of 0.1 mV s^{-1} (a) and GCD profiles of the first three cycles at 0.1 A g^{-1} in the voltage window of 0.01−3 V (b) of NbSe$_2$-M for LIBs.

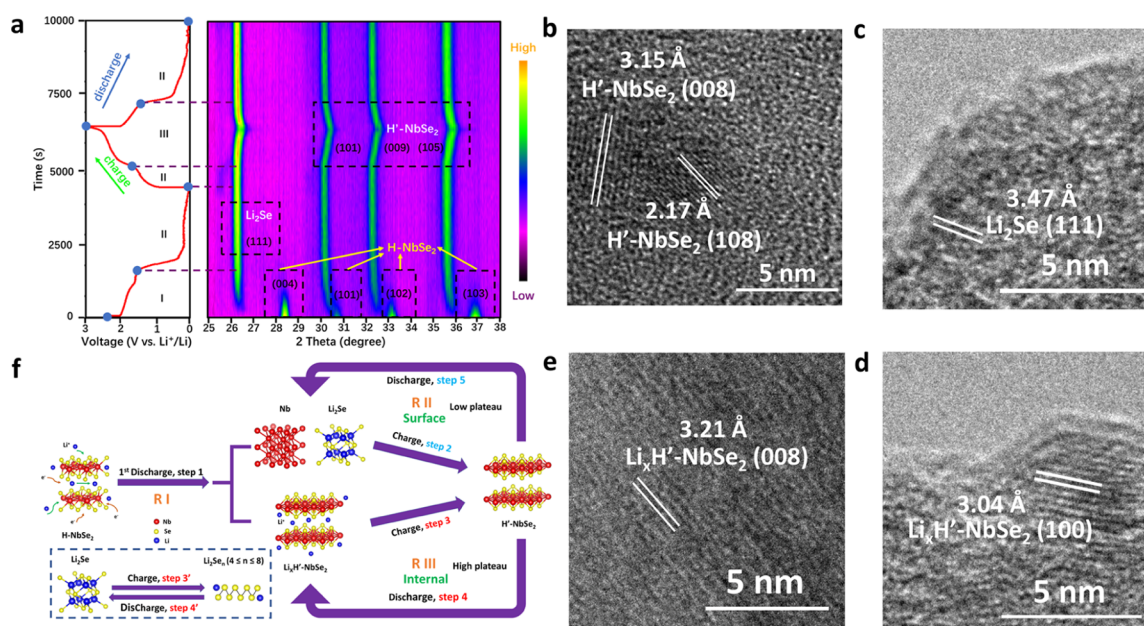**Figure 3.** Li$^+$-storage mechanism of NbSe$_2$-M. (a) In situ XRD measurement and its corresponding GCD profiles at 0.2 A g^{-1} in the voltage window of 0.01−3 V. Ex situ HRTEM after the sample is charged to 3 V (b) and discharged to 0.01 V (c−e) in the second cycle. (f) Schematic illustration of Li$^+$-storage mechanism in the first and second cycles.

■ RESULTS AND DISCUSSION

Structural and Morphological Characterizations of NbSe$_2$ and NbSe$_2$-M. The XRD patterns are all well-indexed to the hexagonal NbSe$_2$ with a space group of $P6_3/mmc$ (194) and a = 3.4446 Å, c = 12.5444 Å (JCPDS no. 01-072-0864, Figure 1a). After microwave treatment, the phase of NbSe$_2$ is unchanged. For a further investigation of the effect of microwave treatment on the internal chemical bonds of NbSe$_2$, Raman spectra were collected. The characteristic peaks located at ~144 and ~237 cm^{-1} correspond to E$_{1g}$ and E$_{2g}$ modes of NbSe$_2$, respectively (Figure 1b).[24,25] The substantial increased density of the peak at the E$_{1g}$ mode suggests the strengthened interlayer bonding.[26] Obviously, compared to that of NbSe$_2$, the peak of the E$_{2g}$ mode of NbSe$_2$-M is broadened, which indicates the smaller crystal size[27] brought by the nanosizing function of microwave (gray rectangular area in Figure 1b). Besides, the down shift of E$_{1g}$ and E$_{2g}$ modes after microwave treatment is caused by the surface stress,[28,29] which probably derives from the recrystallization of the crystal surface. SEM was used to directly observe the morphologies of NbSe$_2$ samples with or without microwave treatment. Without being treated, the material is smooth bulk with the size of 10−

30 μm (Figure S1); after being treated, nanoparticles of <400 nm grow on the surface of the bulk (Figure 1c). TEM images were measured to further observe the micromorphology. Figure 1d shows that the nanoparticles are about 200 nm in length and ~100 nm in width. Figure 1e further displays that there still exists plenty of smaller nanoparticles distributed on the edge of the main body of the NbSe$_2$ nanoparticle. The (004) and (006) atomic planes with a lattice spacing of 3.14 and 2.09 Å of the hexagonal NbSe$_2$ can be clearly observed in the HRTEM images (Figure 1f). Elemental mapping results shown in Figure 1g demonstrate that Nb and Se elements are uniformly distributed in NbSe$_2$-M.

Electrochemical Performance for LIBs. First, Li$^+$-storage performance was investigated via assembling CR2016-type coin cells with NbSe$_2$-M as the cathode, lithium foil as the anode, and LiPF$_6$ as the electrolyte. CV measurements were performed to describe the lithium-storage behavior in a voltage range from 0.01 to 3 V (vs Li$^+$/Li) at the scan rate of 0.1 mV s^{-1} (Figure 2a). In the first discharge process, a broad cathodic peak located at 1.65 V corresponds to the irreversible phase transition (from H−NbSe$_2$ to H′−NbSe$_2$, Table S1) and the conversion of H−NbSe$_2$ revealed by later in situ XRD (Figure

3a). The following relatively sharp reduction peak at 0.63 V can be ascribed to the conversion reaction of H′−NbSe$_2$ confirmed by later in situ XRD and ex situ HRTEM (Figure 3a,b−e) assisted by the previous reported work of selenides.[30,31] The exceedingly sharp cathodic peak at 0.08 V can be attributed to the formation of a solid electrolyte interface on the fresh electrode surface.[30] In the second charge process, a reversible anodic peak at 1.84 V can be assigned to the deintercalation of Li$^+$ from H′−NbSe$_2$ proved by later analysis. The sequential peak located at 2.09 V can be ascribed to the oxidation of Li$_2$Se to polyselenides (Li$_2$Se$_n$, $4 \leq n \leq 8$).[32] In the second discharge process, as the inverse reaction appeared at 1.84 and 2.09 V, a reversible cathodic peak at 1.85 V is attributed to the intercalation of Li$^+$ into H′−NbSe$_2$ and the reduction of polyselenides to Li$_2$Se. Analogously, the sequential two reversible cathodic peaks at 0.83/0.42 V can be attributed to the conversion of H′−NbSe$_2$. The reasons for the ascriptions of peaks in the third cycle resemble those in the second cycle because of the ignorable peak shifts. Obviously, a larger peak area owned by low-potential redox peaks indicates their greater contribution to capacity.[33] GCD profiles at 0.1 A g^{-1} are shown in Figure 2b. NbSe$_2$-M delivers an initial capacity of 569 mA h g^{-1} but decreases to 313 mA h g^{-1} because of the irreversible reactions mentioned in the above discussion. Obviously, three inconspicuous plateaus at ∼1.75/0.75/0.25 V are matched with the three reduction peaks of the first discharge process in the CV curves.

Li$^+$-Storage Mechanism of NbSe$_2$-M with Surface Conversion and Internal Intercalation. In situ XRD was carried out to investigate the mechanism of lithium storage in NbSe$_2$ for the first time. The discharge−charge voltage profiles and potential plateaus have little difference compared to those in Figure 2b, which originates from the different test molds. As shown in Figure 3a, all diffraction peaks of the pristine sample can be well-indexed to the hexagonal NbSe$_2$ (noted as H−NbSe$_2$, JCPDS card no. 01-072-0864). During the discharge process from 2.40 to 1.50 V (noted as stage I) in the first cycle, an apparent discontinuous down shift is observed, indicating a typical heterogeneous reaction.[34] In contrast to the gradually weakened pristine H−NbSe$_2$ phase, new phases whose diffraction peaks are located at ∼26.3°, ∼30.3°, ∼32.4°, and ∼35.8° become strengthened and match well with the cubic Li$_2$Se (JCPDS card no. 00-023-0072) and another hexagonal NbSe$_2$ (noted as H′−NbSe$_2$, JCPDS card no. 01-089-5314), respectively. The above irreversible heterogeneous reaction (noted as RI) includes two processes and can be suggested as

$$H - NbSe_2 + xLi \rightarrow Li_xH' - NbSe_2$$

$$H - NbSe_2 + 4Li \rightarrow 2Li_2Se + Nb \qquad (RI)$$
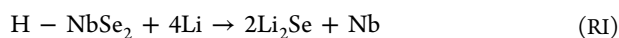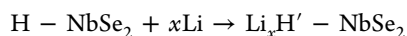
In stage II (1.50−0.01 V in the first discharge and 0.01−1.70 V in the second charge, namely, the low plateau), a little shift is observed, which can be ascribed to the reversible conversion reaction (noted as RII) of H′−NbSe$_2$.[35] Thus, the reaction can be expressed by the following equation

$$Li_xH' - NbSe_2 + (4 - x)Li \leftrightarrow 2Li_2Se + Nb \qquad (RII)$$
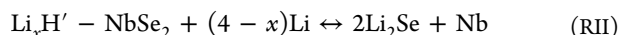
In stage III (1.70−3 V in the second charge and 3−1.40 V in the third discharge, namely, the high plateau), the peaks of H′−NbSe$_2$ continuously move toward higher 2θ angles and then reversibly shift back to their original positions because of the reversible Li$^+$ extraction/insertion in H′−NbSe$_2$.[34] The

reaction (noted as RIII) can be described by the following equation

$$H' - NbSe_2 + xLi \leftrightarrow Li_xH' - NbSe_2 \qquad (RIII)$$
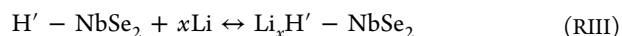
In addition, compared to the obvious shifts of H′−NbSe$_2$, a reversible small peak shift of Li$_2$Se in the narrower voltage window of 1.8−2.2 V is observed, corresponding to the oxidation−reduction reaction between Li$_2$Se and polyselenides.[32] The reversible reaction is suggested as

$$Li_2Se + (n - 1)Se \leftrightarrow Li_2Se_n (4 \leq n \leq 8) \qquad (RIV)$$
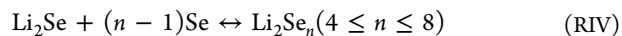
Ex situ HRTEM of the fully discharged−charged materials was carried out to further confirm the reaction product. When charged to 3 V in the second cycle, only single H′−NbSe$_2$ phase exists, as expected in Figure 3b. When discharged to 0.01 V, the lattice fringes of Li$_2$Se can be recognized in Figure 3c, which indicate the conversion reaction between lithium and H′−NbSe$_2$. In addition, a larger interplanar spacing of (100) and (008) planes (3.04 Å vs 2.98 Å and 3.21 Å vs 3.15 Å, namely discharged states vs standard states) in H′−NbSe$_2$ is observed in Figure 3d,e, suggesting that the Li$^+$ ion intercalation into the interlayer of H′−NbSe$_2$ induces the lattice expansion.[17] The above observations further confirm the coexistence of conversion reactions and intercalation reactions of H′−NbSe$_2$ in lithium storage.

The schematic illustration of the heterogeneous reaction mechanism includes the phase transformation of NbSe$_2$ itself in the first cycle, its conversion reaction in the low plateau, as well as the following intercalation reaction and oxidation−reduction reaction between Li$_2$Se and polyselenides in the high plateau, as shown in Figure 3f. Assisted by ex situ SEM, the whole process is clearly recorded (Figure S2). After discharged to 1.65 V in the first cycle, the pristine H−NbSe$_2$ bulk transforms into the size-reduced cubic-shaped H′−NbSe$_2$. When further discharged to 0.01 V, part of the bulk twists and deforms that corresponds to the conversion of H′−NbSe$_2$, and the other well-preserved part is matched with the intercalation reaction, which is similar to the size-controlled intercalation-to-conversion mechanism of lithium storage in NbSe$_3$.[36] When charged back to 3 V, crystallized nanoparticles appear in the position where the deformed part existed, indicating the inverse process.

Electrochemical Performance for MIBs. Mg^{2+}-storage performance was investigated via assembling CR2016-type coin cells with NbSe$_2$ and NbSe$_2$-M as the cathode, Mg metal as the anode, and APC as the electrolyte. Figure 4a,b shows the CV curves and GCD profiles of NbSe$_2$ and NbSe$_2$-M. Apparently, a small capacity of NbSe$_2$ with no plateau is observed. On the contrary, NbSe$_2$-M delivers a high discharge capacity of 101 mA h g^{-1} with a stable discharge plateau of 1.30 V at the current density of 200 mA g^{-1}, corresponding to the energy density of 131.1 W h kg^{-1} (based on the weight of active materials) and 0.47 Mg^{2+} intercalation per formula unit (1e$^-$ transfer ≈ 107 mA h g^{-1}) of NbSe$_2$. The reversible peak pair of 1.77/1.30 V can be assigned to the deintercalation/intercalation of the Mg^{2+} ion, which is proved by subsequent ex situ XRD and ex situ XPS. The relatively great enhancement of Mg^{2+} storage through controlling microwave treatment can be ascribed to the reduced crystal size during the recrystallization of NbSe$_2$. At 50 mA g^{-1}, NbSe$_2$ shows poor cycling performance; on the contrary, even at a high current density of 500 mA g^{-1}, NbSe$_2$-M exhibits much better cycling stability (Figure 4c). In the first cycle, a discharge capacity of 134 mA h
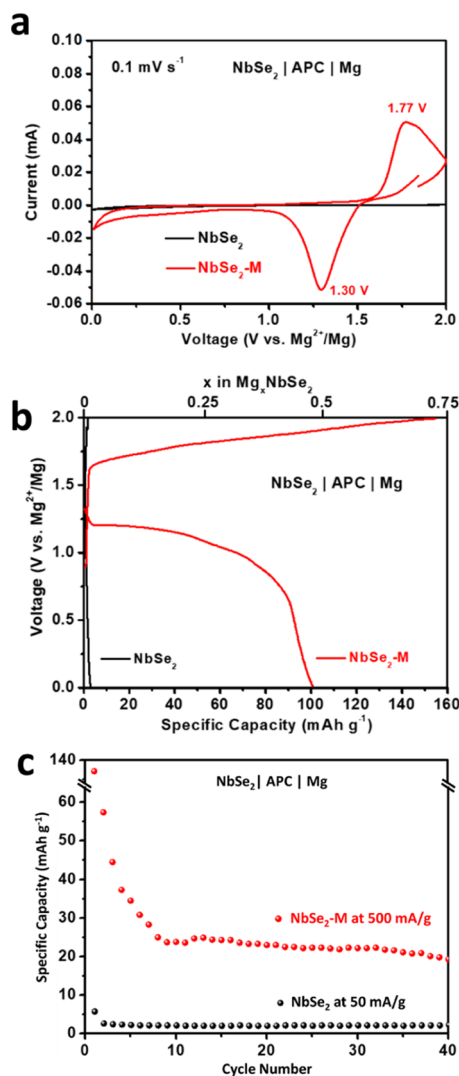
Figure 4. Electrochemical performance of NbSe$_2$ and NbSe$_2$-M for MIBs. (a) CV curves under the scan rate of 0.1 mV s^{-1}. (b) GCD profiles in the voltage window of 0.01−2 V. (c) Cycling performance.

g^{-1} is obtained followed by a rapid capacity fading (decreases to 57 mA h g^{-1}) in the second cycle, which can be attributed to the irreversible insertion/exertion of Mg^{2+} in the first cycle. This phenomenon can also be observed in Figure S3. In the first cycle, a broad cathodic peak at 0.74 V corresponds the Mg^{2+} intercalation into NbSe$_2$-M hosts and other irreversible side reactions.[37] In the following cycles, the capacity of NbSe$_2$-M gets decreased because of the strong polarization of Mg^{2+}, which is derived from its bivalent nature that leads to a strong electrostatic interaction with the host ions during the insertion/deinsertion process.[38] EDS mappings of the Mg element before (blank group) and after the GCD test further explain the insertion of Mg^{2+} into NbSe$_2$-M host because of the relative increase of the Mg signal at the same situation (Figure S4). The diffusivity coefficient of Mg^{2+} in NbSe$_2$-M is calculated between 3.06×10^{-8} to 3.17×10^{-6} cm^2 s^{-1} by galvanostatic intermittent titration technique measurements (Figure S5).[39] Comparison of the reported cathode materials in the discharge plateau versus the specific capacity for coin-type MIBs with APC as the electrolyte and Mg metal as the anode is shown in Figure S6. Compared with other cathode materials, whether TMDCs,[15−17] Mo$_6$S$_8$ CPs,[40] or vanadium-

based or titanium-based layered oxides,[37,41,42] NbSe$_2$-M shows the highest discharge plateau of 1.30 V and a good specific energy density of 131.1 W h kg^{-1} (Table S2).

Mechanism of Reversible Intercalation of Mg^{2+} in NbSe$_2$-M. Ex situ XRD was used to explore the Mg^{2+}-storage mechanism of NbSe$_2$-M for the first time, which exhibits a completely different structural change behavior compared with that in LIBs (Figure 5a). First, during the discharge of the initial cycle, a continuous but slow successive down shift is observed, indicating the Mg^{2+} insertion into H−NbSe$_2$ (Figure 5a,d). It is worth noting that strong peaks at ~14.2° and ~41.7° indexed to (002) and (104) planes resist the inescapable rising potential and move to lower 2θ angles, but another strong peak at ~43.2° matched to the (005) plane succumbs and moves much slowly, which may be associated with the intrinsic properties of planes and their orientation change caused by Mg^{2+} intercalation (Figure 5b,c). In the second cycle, all diffraction peaks of H−NbSe$_2$ first shift toward higher 2θ angles during charge and reversibly move back to their original positions, which can be ascribed to the continuous lattice contraction and expansion caused by Mg^{2+} extraction and insertion.[36] In addition, three peaks located at ~18.2°, ~22.5°, and ~26.7° are well-indexed to the binder PTFE (JCPDS card no. 00-054-1595), precipitated MgCl$_2$ (JCPDS card no. 01-070-2746), and the conductive agent acetylene black (JCPDS card no. 00-026-1076), respectively. Ex situ XPS of the fully discharged−charged sample was taken to further confirm the valence states of Nb and Se elements in the reaction product. When charged to 2 V in the second cycle, the peaks at 210.2 and 207.3 eV can be attributed to Nb^{4+};[43] and the peaks located at 205.8 and 203.1 eV can be ascribed to Nb^{3+}[44] because the irreversible capacity loss that leads to Nb^{4+} are not fully reduced to Nb^{3+} (Figure 5e). When discharged to 0.01 V, only small down shifts of these peaks within 0.3 eV are observed, indicating the uncharged valence states of Nb (Figure 5f). However, the ratio of the peak area of Nb^{3+}/Nb^{4+} gets larger, suggesting the further reduction of Nb^{4+}. As for the Se element, down shifts of the peaks at 53.7 and 53.0 eV are less than 0.3 eV, corresponding to the constant Se^{2-} (Figure 5g,h).[45] In addition, strong peaks of Cl 2p[46] and Mg 2p[47] appear because the precipitated MgCl$_2$ originated from the APC electrolyte (Figure 5e−h). The results of XPS further demonstrate the Mg^{2+} extraction/insertion into H−NbSe$_2$.

Electrochemical Performance for MLHBs and the Lithium−Magnesium Cointercalation Behavior. To further improve the capacity and cycling stability of NbSe$_2$-M in MIBs, introducing lithium salt (such as LiCl) into the APC electrolyte has been proved to be an effective way to reduce the strong polarization of Mg^{2+} for the priority of Li$^+$ species competing with Mg^{2+} species based on faster intercalation dynamics.[48−50] As a result, MLHBs were assembled with NbSe$_2$-M as the cathode, Mg metal as the anode, and 1 M LiCl in 0.25 M APC as the electrolyte. CV curves of the initial three cycles are shown in Figure S7a. According to the above conclusion of lithium and magnesium storage mechanisms, the peak at 1.15 V (vs Mg^{2+}/Mg) in the first discharge can be assigned to the phase transition and conversion of H−NbSe$_2$ as well as the Mg^{2+} intercalation and other irreversible side reactions. The sequential oxidation peaks at 1.36 and 1.71 V correspond to the Li$^+$ and Mg^{2+} deintercalation into NbSe$_2$-M host, respectively. The cathodic peak at 1.25 V can be ascribed to the cointercalation of Li$^+$ and Mg^{2+} because of the adjacent Mg^{2+} intercalation potential of

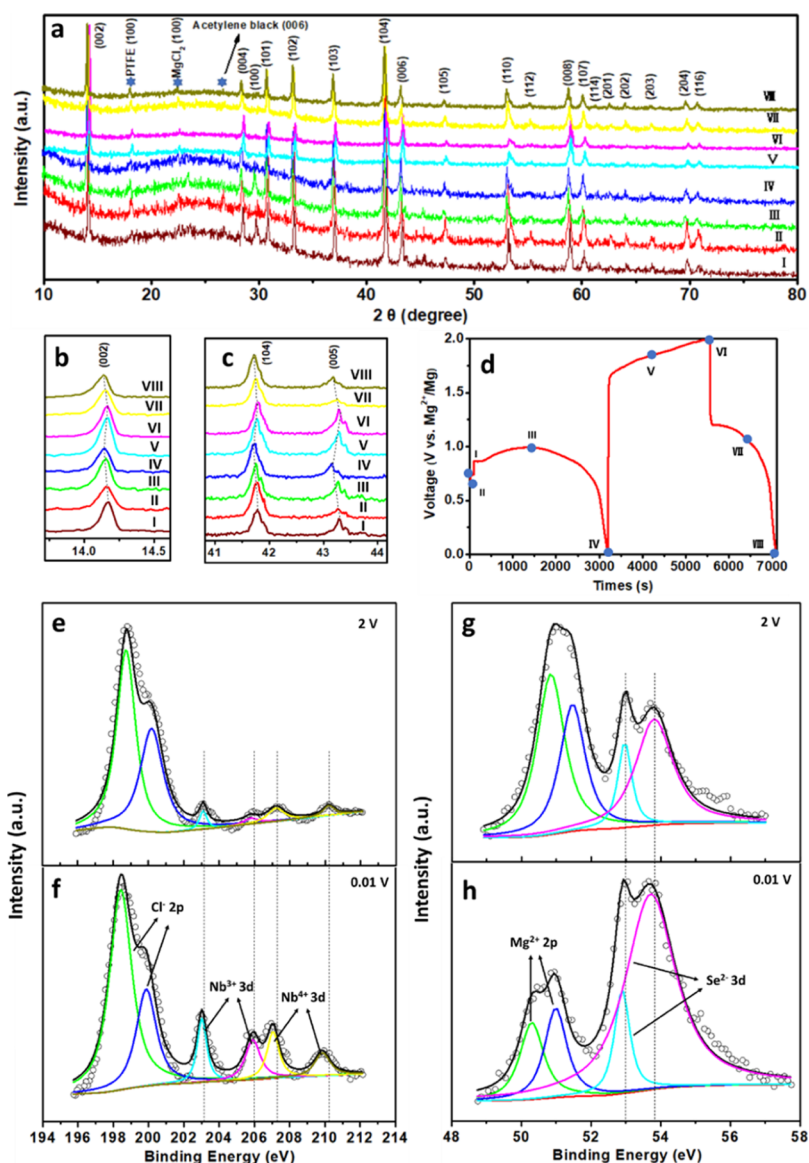**Figure 5.** Mechanism of reversible intercalation of Mg^{2+} in $NbSe_2$-M. (a–c) Ex situ XRD measurements and its enlarged drawing of (002), (104), and (005) planes. (d) Corresponding GCD profiles. (e–h) Ex situ XPS spectra of Nb and Se elements when the sample is charged to 2 V and discharged to 0.01 V in the second cycle.

1.30 V and the Li^+ intercalation potential of 1.27 V (vs Mg^{2+}/Mg) in the second discharge. In addition, the lower potential (below 0.5 V) peaks are related to the conversion reaction between lithium and $NbSe_2$-M because almost no peaks below 0.5 V in MIBs are observed. Compared with pure Mg^{2+} insertion/extraction, Mg^{2+}/Li^+ cointercalation delivers higher capacity of 123 mA h g^{-1} and much better sustained capacity of ~47 mA h g^{-1} at 100 mA g^{-1} after 100 cycles, ~37 mA h g^{-1} at 200 mA g^{-1} after 200 cycles, and ~26 mA h g^{-1} at 500 mA g^{-1} after 300 cycles (Figure S7b,c).

CONCLUSIONS

In summary, we have developed a novel hexagonal $NbSe_2$ with a nanosized surface by a simple and effective microwave–hydrothermal method. The Li^+-storage mechanism of $NbSe_2$ with surface conversion at a low plateau and internal intercalation at a high plateau after the irreversible phase transition in the first cycle is revealed. The different ion-storage mechanisms in the surface and internal phase can be ascribed

to the size of $NbSe_2$, bringing distinct mechanical and chemical effects when the Li^+ ions enter the host. Besides, Mg^{2+} intercalation mechanism is also confirmed. As the cathode for MIBs, it exhibits a high rate capacity of 101 mA h g^{-1} at 200 mA g^{-1} with a high discharge plateau of 1.30 V in the system of coin-type batteries consisting of APC as the electrolyte and Mg metal as the anode. The above findings build a deep understanding of ion-storage mechanisms in TMDCs and provide guidance for designing new electrode materials with high electrochemical performances.

ASSOCIATED CONTENT

Ⓢ Supporting Information

The Supporting Information is available free of charge on the ACS Publications website at DOI: 10.1021/acsami.8b12662.

SEM image of $NbSe_2$ bulk; ex situ SEM of $NbSe_2$-M at different states for LIBs; CV curves of the initial three cycles under the scan rate of 0.1 mV s^{-1} of $NbSe_2$-M for MIBs; comparison of the reported cathode materials in

the discharge plateau versus specific capacity for coin-type MIBs with APC as the electrolyte and Mg metal as the anode; electrochemical performance of NbSe$_2$-M for MLHBs; differences between H−NbSe$_2$ and H′−NbSe$_2$; and comparison of the reported cathode materials in specific capacity and discharge plateau for coin-type MIBs with APC as the electrolyte and Mg metal as the anode (PDF)

■ AUTHOR INFORMATION

Corresponding Authors
*E-mail: anqinyou86@whut.edu.cn (Q.A.).
*E-mail: mlq518@whut.edu.cn (L.M.).

ORCID
Liqiang Mai: 0000-0003-4259-7725

Author Contributions
C.P. and H.L. have contributed equally. The manuscript was written through contributions of all authors. All authors have given approval to the final version of the manuscript.

Notes
The authors declare no competing financial interest.

■ REFERENCES

(1) Dunn, B.; Kamath, H.; Tarascon, J.-M. Electrical Energy Storage for the Grid: A Battery of Choices. *Science* **2011**, *334*, 928−935.

(2) Yang, Z.; Zhang, J.; Kintner-Meyer, M. C. W.; Lu, X.; Choi, D.; Lemmon, J. P.; Liu, J. Electrochemical Energy Storage for Green Grid. *Chem. Rev.* **2011**, *111*, 3577−3613.

(3) Larcher, D.; Tarascon, J.-M. Towards Greener and More Sustainable Batteries for Electrical Energy Storage. *Nat. Chem.* **2015**, *7*, 19−29.

(4) You, Y.; Manthiram, A. Progress in High-Voltage Cathode Materials for Rechargeable Sodium-Ion Batteries. *Adv. Energy Mater.* **2018**, *8*, 1701785.

(5) You, Y.; Kim, S. O.; Manthiram, A. A Honeycomb-Layered Oxide Cathode for Sodium-Ion Batteries with Suppressed P3-O1 Phase Transition. *Adv. Energy Mater.* **2017**, *7*, 1601698.

(6) Tarascon, J.-M.; Armand, M. Issues and Challenges Facing Rechargeable Lithium Batteries. *Nature* **2001**, *414*, 359−367.

(7) Etacheri, V.; Marom, R.; Elazari, R.; Salitra, G.; Aurbach, D. Challenges in the Development of Advanced Li-Ion Batteries: A Review. *Energy Environ. Sci.* **2011**, *4*, 3243−3262.

(8) Wu, N.; Lyu, Y.-C.; Xiao, R.-J.; Yu, X.; Yin, Y.-X.; Yang, X.-Q.; Li, H.; Gu, L.; Guo, Y.-G. A Highly Reversible, Low-Strain Mg-Ion Insertion Anode Material for Rechargeable Mg-Ion Batteries. *NPG Asia Mater.* **2014**, *6*, No. e120.

(9) Wang, W.; Liu, L.; Wang, P.-F.; Zuo, T.-T.; Yin, Y.-X.; Wu, N.; Zhou, J.-M.; Wei, Y.; Guo, Y.-G. A Novel Bismuth-Based Anode Material with a Stable Alloying Process by the Space Confinement of an in Situ Conversion Reaction for a Rechargeable Magnesium Ion Battery. *Chem. Commun.* **2018**, *54*, 1714−1717.

(10) Aurbach, D.; Lu, Z.; Schechter, A.; Gofer, Y.; Gizbar, H.; Turgeman, R.; Cohen, Y.; Moshkovich, M.; Levi, E. Prototype Systems for Rechargeable Magnesium Batteries. *Nature* **2000**, *407*, 724−727.

(11) Muldoon, J.; Bucur, C. B.; Gregory, T. Quest for Nonaqueous Multivalent Secondary Batteries: Magnesium and Beyond. *Chem. Rev.* **2014**, *114*, 11683−11720.

(12) Chang, K.; Chen, W. L-Cysteine-Assisted Synthesis of Layered MoS$_2$/Graphene Composites with Excellent Electrochemical Performances for Lithium Ion Batteries. *ACS Nano* **2011**, *5*, 4720−4728.

(13) Jing, Y.; Zhou, Z.; Cabrera, C. R.; Chen, Z. Metallic VS$_2$ Monolayer: A Promising 2D Anode Material for Lithium Ion Batteries. *J. Phys. Chem. C* **2013**, *117*, 25409−25413.

(14) Yoder, T. S.; Tussing, M.; Cloud, J. E.; Yang, Y. Resilient Carbon Encapsulation of Iron Pyrite (FeS$_2$) Cathodes in Lithium Ion Batteries. *J. Power Sources* **2015**, *274*, 685−692.

(15) Sun, X.; Bonnick, P.; Nazar, L. F. Layered TiS$_2$ Positive Electrode for Mg Batteries. *ACS Energy Lett.* **2016**, *1*, 297−301.

(16) Sun, X.; Bonnick, P.; Duffort, V.; Liu, M.; Rong, Z.; Persson, K. A.; Ceder, G.; Nazar, L. F. A High Capacity Thiospinel Cathode for Mg Batteries. *Energy Environ. Sci.* **2016**, *9*, 2273−2277.

(17) Liang, Y.; Yoo, H. D.; Li, Y.; Shuai, J.; Calderon, H. A.; Robles Hernandez, F. C.; Grabow, L. C.; Yao, Y. Interlayer-Expanded Molybdenum Disulfide Nanocomposites for Electrochemical Magnesium Storage. *Nano Lett.* **2015**, *15*, 2194−2202.

(18) Yokoya, T.; Kiss, T.; Chainani, A.; Shin, S.; Nohara, M.; Takagi, H. Fermi Surface Sheet-Dependent Superconductivity in 2H-NbSe$_2$. *Science* **2001**, *294*, 2518−2520.

(19) Xi, X.; Wang, Z.; Zhao, W.; Park, J.-H.; Law, K. T.; Berger, H.; Forró, L.; Shan, J.; Mak, K. F. Ising Pairing in Superconducting NbSe$_2$ Atomic Layers. *Nat. Phys.* **2016**, *12*, 139−143.

(20) Xi, X.; Zhao, L.; Wang, Z.; Berger, H.; Forró, L.; Shan, J.; Mak, K. F. Strongly Enhanced Charge-Density-Wave Order in Monolayer NbSe$_2$. *Nat. Nanotechnol.* **2015**, *10*, 765−769.

(21) Weber, F.; Rosenkranz, S.; Castellan, J.-P.; Osborn, R.; Hott, R.; Heid, R.; Bohnen, K.-P.; Egami, T.; Said, A. H.; Reznik, D. Extended Phonon Collapse and the Origin of the Charge-Density Wave in 2H-Nbse$_2$. *Phys. Rev. Lett.* **2011**, *107*, 107403.

(22) Lv, X.; Wei, W.; Sun, Q.; Huang, B.; Dai, Y. A First-Principles Study of Nbse$_2$ Monolayer as Anode Materials for Rechargeable Lithium-Ion and Sodium-Ion Batteries. *J. Phys. D: Appl. Phys.* **2017**, *50*, 235501.

(23) Hitz, E.; Wan, J.; Patel, A.; Xu, Y.; Meshi, L.; Dai, J.; Chen, Y.; Lu, A.; Davydov, A. V.; Hu, L. Electrochemical Intercalation of Lithium Ions into NbSe$_2$ Nanosheets. *ACS Appl. Mater. Interfaces* **2016**, *8*, 11390−11395.

(24) Sooryakumar, R.; Klein, M. V.; Frindt, R. F. Effect of Nonmagnetic Impurities on the Raman Spectra of the Superconductor Niobium Diselenide. *Phys. Rev. B: Condens. Matter Mater. Phys.* **1981**, *23*, 3222−3229.

(25) Staley, N. E.; Wu, J.; Eklund, P.; Liu, Y.; Li, L.; Xu, Z. Electric Field Effect on Superconductivity in Atomically Thin Flakes of Nbse$_2$. *Phys. Rev. B: Condens. Matter Mater. Phys.* **2009**, *80*, 184505.

(26) Wang, C. S.; Chen, J. M. Raman Spectrum of Metallic Layered Compound NbSe$_2$. *Solid State Commun.* **1974**, *14*, 1145−1148.

(27) Maira, A. J.; Yeung, K. L.; Lee, C. Y.; Yue, P. L.; Chan, C. K. Size Effects in Gas-Phase Photo-Oxidation of Trichloroethylene Using Nanometer-Sized TiO$_2$ Catalysts. *J. Catal.* **2000**, *192*, 185−196.

(28) Englert, T.; Abstreiter, G.; Pontcharra, J. Determination of Existing Stress in Silicon Films on Sapphire Substrate Using Raman Spectroscopy. *Solid-State Electron.* **1980**, *23*, 31−33.

(29) De Wolf, I. Stress Measurements in Si Microelectronics Devices Using Raman Spectroscopy. *J. Raman Spectrosc.* **1999**, *30*, 877−883.

(30) Wang, H.; Wang, X.; Wang, L.; Wang, J.; Jiang, D.; Li, G.; Zhang, Y.; Zhong, H.; Jiang, Y. Phase Transition Mechanism and Electrochemical Properties of Nanocrystalline MoSe$_2$ as Anode Materials for the High Performance Lithium-Ion Battery. *J. Phys. Chem. C* **2015**, *119*, 10197−10205.

(31) Zhou, T.; Pang, W. K.; Zhang, C.; Yang, J.; Chen, Z.; Liu, H. K.; Guo, Z. Enhanced Sodium-Ion Battery Performance by Structural Phase Transition from Two-Dimensional Hexagonal-SnS_2 to Orthorhombic-SnS. *ACS Nano* **2014**, *8*, 8323−8333.

(32) Mukkabla, R.; Deshagani, S.; Meduri, P.; Deepa, M.; Ghosal, P. Selenium/Graphite Platelet Nanofiber Composite for Durable Li-Se Batteries. *ACS Energy Lett.* **2017**, *2*, 1288−1295.

(33) Zhang, J.; Du, C.; Dai, Z.; Chen, W.; Zheng, Y.; Li, B.; Zong, Y.; Wang, X.; Zhu, J.; Yan, Q. NbS_2 Nanosheets with M/Se (M = Fe, Co, Ni) Codopants for Li^+ and Na^+ Storage. *ACS Nano* **2017**, *11*, 10599−10607.

(34) Yue, J.-L.; Zhou, Y.-N.; Shi, S.-Q.; Shadike, Z.; Huang, X.-Q.; Luo, J.; Yang, Z.-Z.; Li, H.; Gu, L.; Yang, X.-Q.; Fu, Z.-W. Discrete Li-Occupation Versus Pseudo-Continuous Na-Occupation and Their Relationship with Structural Change Behaviors in $Fe_2(MoO_4)_3$. *Sci. Rep.* **2015**, *5*, 8810.

(35) Permien, S.; Indris, S.; Schürmann, U.; Kienle, L.; Zander, S.; Doyle, S.; Bensch, W. What Happens Structurally and Electronically During the Li Conversion Reaction of $CoFe_2O_4$ Nanoparticles: an Operando XAS and XRD Investigation. *Chem. Mater.* **2016**, *28*, 434−444.

(36) Luo, L.; Zhao, B.; Xiang, B.; Wang, C.-M. Size-Controlled Intercalation-to-Conversion Transition in Lithiation of Transition-Metal Chalcogenides-$NbSe_3$. *ACS Nano* **2016**, *10*, 1249−1255.

(37) Rashad, M.; Zhang, H.; Asif, M.; Feng, K.; Li, X.; Zhang, H. Low-Cost Room-Temperature Synthesis of $NaV_3O_8 \cdot 1.69H_2O$ Nanobelts for Mg Batteries. *ACS Appl. Mater. Interfaces* **2018**, *10*, 4757−4766.

(38) Saha, P.; Datta, M. K.; Velikokhatnyi, O. I.; Manivannan, A.; Alman, D.; Kumta, P. N. Rechargeable Magnesium Battery: Current Status and Key Challenges for the Future. *Prog. Mater. Sci.* **2014**, *66*, 1−86.

(39) Sheng, J.; Peng, C.; Xu, Y.; Lyu, H.; Xu, X.; An, Q.; Mai, L. $KTi_2(PO_4)_3$ with Large Ion Diffusion Channel for High-Efficiency Sodium Storage. *Adv. Energy Mater.* **2017**, *7*, 1700247.

(40) Muthuraj, D.; Mitra, S. Reversible Mg Insertion into Chevrel Phase Mo_6S_8 Cathode: Preparation, Electrochemistry and X-Ray Photoelectron Spectroscopy Study. *Mater. Res. Bull.* **2018**, *101*, 167−174.

(41) Miao, X.; Chen, Z.; Wang, N.; Nuli, Y.; Wang, J.; Yang, J.; Hirano, S.-i. Electrospun V_2MoO_8 as a Cathode Material for Rechargeable Batteries with Mg Metal Anode. *Nano Energy* **2017**, *34*, 26−35.

(42) Meng, Y.; Wang, D.; Wei, Y.; Zhu, K.; Zhao, Y.; Bian, X.; Du, F.; Liu, B.; Gao, Y.; Chen, G. Ultrathin TiO_2-B Nanowires as an Anode Material for Mg-Ion Batteries Based on a Surface Mg Storage Mechanism. *J. Power Sources* **2017**, *346*, 134−142.

(43) Kim, S.-J.; Bae, H.-S.; Yee, K.-A.; Choy, J.-H.; Kim, D.-K.; Hur, N.-H. Structure and Physical Properties of the Barium Niobium Sulfides $BaNbS_3$ and $BaNb_{0.8}S_{3-\delta}$. *J. Solid State Chem.* **1995**, *115*, 427−434.

(44) Darlinski, A.; Halbritter, J. Angle-Resolved XPS Studies of Oxides at NbN, NbC, and Nb Surfaces. *Surf. Interface Anal.* **1987**, *10*, 223−237.

(45) Nelson, A. J.; Swartzlander, A. B.; Tuttle, J. R.; Noufi, R.; Patel, R.; Höchst, H. Photoemission Investigation of the Electronic Structure at Polycrystalline $CuInSe_2$ Thin-Film Interfaces. *J. Appl. Phys.* **1993**, *74*, 5757−5760.

(46) Magni, E.; Somorjai, G. A. Preparation of a Model Ziegler-Natta Catalyst: Electron Irradiation Induced Titanium Chloride Deposition on Magnesium Chloride Thin Films Grown on Gold. *Surf. Sci.* **1996**, *345*, 1−16.

(47) Hoogewijs, R.; Fiermans, L.; Vennik, J. Electronic relaxation processes in the KLL′ auger spectra of the free magnesium atom, solid magnesium and MgO. *J. Electron Spectrosc. Relat. Phenom.* **1977**, *11*, 171−183.

(48) Gofer, Y.; Chusid, O.; Gizbar, H.; Viestfrid, Y.; Gottlieb, H. E.; Marks, V.; Aurbach, D. Improved Electrolyte Solutions for Rechargeable Magnesium Batteries. *Electrochem. Solid-State Lett.* **2006**, *9*, A257−A260.

(49) Sun, R.; Pei, C.; Sheng, J.; Wang, D.; Wu, L.; Liu, S.; An, Q.; Mai, L. High-Rate and Long-Life VS_2 Cathodes for Hybrid Magnesium-Based Battery. *Energy Storage Mater.* **2018**, *12*, 61−68.

(50) Wu, N.; Yang, Z.-Z.; Yao, H.-R.; Yin, Y.-X.; Gu, L.; Guo, Y.-G. Improving the Electrochemical Performance of the $Li_4Ti_5O_{12}$ Electrode in a Rechargeable Magnesium Battery by Lithium-Magnesium Co-Intercalation. *Angew. Chem., Int. Ed.* **2015**, *54*, 5757−5761.